 © Authors of the article / Authors of the article

ГЕОЛОГИЯ, ПОИСКИ И РАЗВЕДКА ТВЕРДЫХ ПОЛЕЗНЫХ ИСКОПАЕМЫХ, МИНЕРАГЕНИЯ/GEOLOGY, PROSPECTING AND EXPLORATION OF SOLID MINERALS, MINERALOGY

DOI: https://doi.org/10.60797/GEO.2026.9.1 EDN: CEQHOR

INTEGRATED REMOTE SENSING AND MINERALOGICAL CHARACTERIZATION OF URANIUM OCCURRENCES IN THE NAMAYENI AREA, MKUJU RIVER, TANZANIA

Research article

Souheib B.[1,] *, Mtui J.[2], Kitinga M.[3]
[1] ORCID : 0009-0008-7230-7630;
[1, 2, 3] Peoples' Friendship University of Russia named after Patrice Lumumba, Moscow, Russian Federation

* Corresponding author (bouzibatsouhaib98[at]gmail.com)

Suggested: 20.05.2026; Accepted: 18.08.2026; Published: 13.11.2026

Abstract

Relevance and the purpose of the work. Uranium is currently considered the energy source with no emissions. Potential presence of uranium deposits has been observed in Tanzania but remains under-explored. Uranium is located in roll-front mineralization in the sandstones of the Namayeni area, Mkuju River Basin, Ruvuma Region. Remote sensing has never been applied in surface alterations or structural mapping there before. The study was conducted with this aim.

Methods of research. Landsat 8 OLI images (Path 165/Row 063, Col2) and SRTM 1" DEM were analyzed in QGIS 3.34 LTR. Reflectance was calculated from raw values following USGS Col2 recommendations, vegetation was masked using NDVI ≥ 0.30 (dry season histogram). Ratios were derived: IOI = B6/B5,CMI = B6/B7,CBI = B7/B6. Lineaments were mapped from RGB hillshades using a multi-azimuth approach, lineament density was also assessed by applying Kernel Density technique. Four normalized layers were combined into the Integrated Uranium Prospectivity Index (IUPI = 0.35 * IOI_norm + 0.30 * CMI_norm + 0.20 * CBI_norm + 0.15 * LineDens_norm). Mineralogical assessment was performed by means of optical microscopy, SEM-EDS and EPMA methods.

Results of the work. According to NDVI analysis, the Namayeni dry season has >97% barren ground, which confirms the validity of spectral indices analysis in such cases. Iron oxide anomalies (IO-1 to IO-5,IOI 1.0–1.7), clay alteration zones (CA-1 to CA-3,CMI 0.8–1.5), carbonate anomalies (CB-1 to CB-3,CBI 0.6–1.2) were revealed. Lineaments are predominantly oriented along the NW-SE direction (~316°) and NE-SW (045–060°),15–20 lineament density peaks are present in the north-central area.

Conclusion. In the north-central Namayeni, associations of iron oxide enrichment, clay alteration, carbonate reaction and structural lineaments have been revealed, which may be considered as the most interesting zones for exploration. Spectral and structural analysis corresponds to typical zoning during roll-front oxidation of sandstone. Analysis was performed in free QGIS software using open access Landsat 8 OLI satellite images.

Keywords: uranium exploration, roll-front mineralization, Landsat 8 OLI, QGIS, spectral indices, lineament analysis, uranium prospectivity mapping, Karoo Supergroup, Mkuju River Basin, Tanzania.

КОМПЛЕКСНОЕ ДИСТАНЦИОННОЕ ЗОНДИРОВАНИЕ И МИНЕРАЛОГИЧЕСКАЯ ХАРАКТЕРИСТИКА ПРОЯВЛЕНИЙ УРАНА В РАЙОНЕ НАМАЙЕНИ, РЕКА МКУДЖУ, ТАНЗАНИЯ

Научная статья

Сухейб Б.[1,] *, Мтуи Ж.[2], Китинга М.[3]
[1] ORCID : 0009-0008-7230-7630;
[1, 2, 3] Российский университет дружбы народов имени Патриса Лумумбы, Москва, Российская Федерация

* Корреспондирующий автор (bouzibatsouhaib98[at]gmail.com)

Предложена: 20.05.2026; Принята: 18.08.2026; Опубликована: 13.11.2026

Аннотация

Актуальность и цель работы. В настоящее время уран рассматривается как источник энергии, не требующий выбросов в атмосферу. В Танзании обнаружено потенциальное присутствие месторождений урана, но они остаются недостаточно изученными. Уран находится в виде рулонной минерализации в песчаниках района Намайени, бассейн реки Мкуджу, регион Рувума. Дистанционное зондирование никогда ранее не применялось для изучения изменений поверхности или структурного картографирования. Исследование было проведено с этой целью.

Методы исследования. Снимки Landsat 8 OLI (траектория 165/строка 063, Col2) и SRTM 1" DEM были проанализированы в QGIS объемом 3,34 LTR. Коэффициент отражения был рассчитан на основе исходных значений в соответствии с рекомендациями USGS Col2,растительность была замаскирована с использованием NDVI ≥ 0,30 (гистограмма сухого сезона). Были получены соотношения: IOI = B6/B5,CMI = B6/B7,CBI = B7/B6. Линеаменты были нанесены на карту по оттенкам холмов RGB с использованием многоазимутального подхода, плотность линеаментов также была оценена с использованием метода плотности ядра. Четыре нормализованных слоя были объединены в Интегральный индекс перспективности на уран (IUPI = 0,35 * IOI_НОРМА + 0,30 * CMI_НОРМА + 0,20 * CBI_НОРМА + 0,15 * Linedens_норма). Минералогическая оценка проводилась с помощью методов оптической микроскопии, СЭМ-ЭДС и ЕРМА.

 © Authors of the article / Authors of the article

Результаты работы. Согласно анализу NDVI, в сухой сезон в Намайени более 97% почвы бесплодно, что подтверждает достоверность анализа спектральных показателей в таких случаях. Выявлены аномалии оксидов железа (от IO-1 до IO-5,IOI 1,0–1,7), зоны изменения глинистости (от CA-1 до CA-3,CMI 0,8–1,5), карбонатные аномалии (от CB-1 до CB-3,CBI 0,6–1,2). Линеаменты преимущественно ориентированы в направлении с северо-запада на юго-восток (~316°) и с северо-запада на юго-запад (045-060°), в северо-центральной области наблюдается 15-20 пиков плотности линеаментов.

Вывод. В северо-центральной части Намайени были выявлены ассоциации с обогащением оксидом железа, изменением состава глины, карбонатной реакцией и структурными линеаментами, которые могут рассматриваться как наиболее интересные зоны для исследования. Спектральный и структурный анализ соответствует типичному районированию при фронтальном окислении песчаника. Анализ проводился в бесплатном программном обеспечении QGIS с использованием спутниковых снимков Landsat 8 OLI в открытом доступе.

Ключевые слова: разведка урана, фронтальная минерализация, Landsat 8 OLI, QGIS, спектральные индексы, линеаментный анализ, картирование перспективности урана, супергруппа Кару, бассейн реки Мкуджу, Танзания.

Introduction

Uranium is the primary fuel for nuclear fission reactors, which at present supply approximately 10% of global electricity generation and are projected to expand considerably as nations pursue decarbonisation targets [1]. International supply is concentrated among a small number of producer countries — Kazakhstan, Canada, Namibia, Australia, and Uzbekistan collectively account for more than 80% of world output [1] — yet the geological distribution of uranium resources is far wider. Sub-Saharan Africa hosts numerous sedimentary basins with documented uranium occurrences that remain incompletely explored, including deposits in Tanzania, Malawi, Zambia, and Niger (Fig. 1).

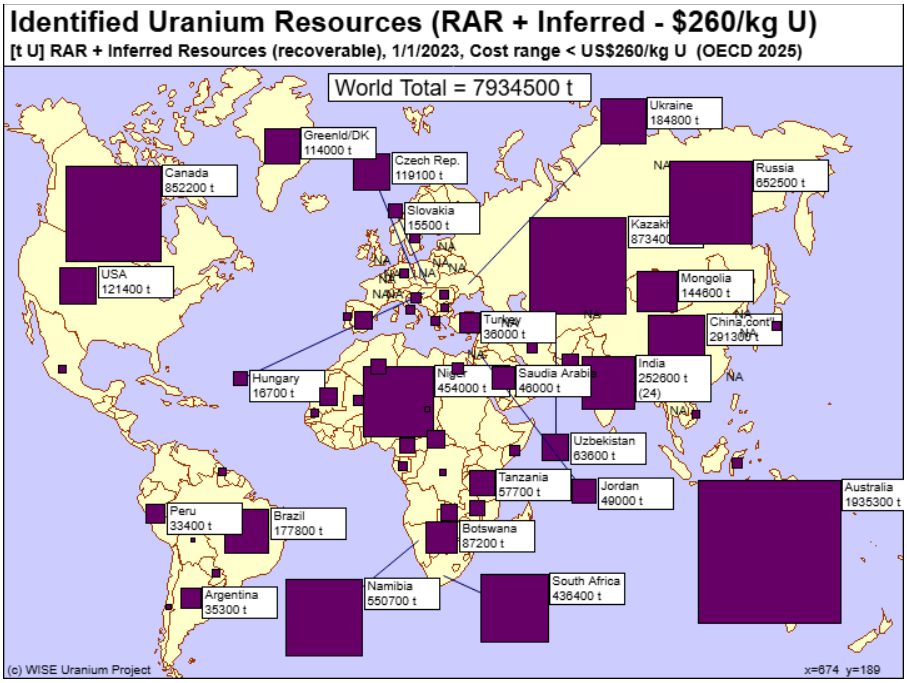


Figure 1 - Global distribution of identified uranium resources (RAR + Inferred, recovery cost < US$260/kg U)
DOI: https://doi.org/10.60797/GEO.2026.9.1.1

Note: source: OECD/NEA – WISE Uranium Project, 2025 [1]

Tanzania occupies a geologically privileged position. Its territory encompasses Archaean cratons flanked by Proterozoic orogenic belts — the Ubendian Belt (2.1–1.8 Ga), the Mozambique Belt (1.0–0.5 Ga), and the Kibaran Belt (1.4–0.9 Ga) — that are composed of granites and migmatites enriched in uranium relative to the cratonic basement [2]. Overlying this Precambrian fabric are Permo-Triassic Karoo intracontinental rift basins formed during Gondwana fragmentation, and Cenozoic structures of the East African Rift System (EARS) [3], [4]. The Mkuju River uranium project in the Ruvuma Region, hosted in sandstones of the Karoo Supergroup, constitutes the most advanced uranium resource in the country [5].

Within this province, the Namayeni exploration block has been subject only to regional geological mapping and reconnaissance-level radiometric surveys. No integrated study combining multispectral satellite remote sensing with detailed uranium mineralogy has previously been published for this block. This knowledge gap is scientifically significant because roll-front uranium deposits generate a characteristic surface alteration zonation — oxidized, transitional, and reduced facies — that produces identifiable spectral signatures in the shortwave-infrared (SWIR) bands of Landsat 8 OLI [6], [7]. Iron oxide enrichment (hematite, goethite, jarosite) in the oxidized zone, clay mineral accumulation (kaolinite, illite) in the transition zone, and carbonate precipitation along redox boundaries have all been exploited as spectral proxies for roll-front

 © Authors of the article / Authors of the article

mineralization in analogous international settings [7], [8]. Structural control via fault-guided groundwater flow adds a further dimension that can be mapped from DEM-derived lineament analysis [9].

The present study addresses the identified gap with four specific objectives:

1) map iron oxide, clay mineral, and carbonate alteration zones using Landsat 8 OLI spectral indices;

2) delineate structural lineaments and compute a lineament density surface from SRTM DEM data;

3) integrate these four datasets into the Integrated Uranium Prospectivity Index (IUPI);

4) characterize the uranium mineral assemblage from drill-core material. Results are contextualized against comparable roll-front deposits in Kazakhstan, the United States Colorado Plateau, and the Kayelekera deposit in Malawi.

Study Area and Geological Setting

2.1. Regional tectonic framework

Tanzania sits at the intersection of several major crustal provinces (Fig. 2). The stable Tanzania Craton (Archaean, ~2.5 Ga) is enclosed by Proterozoic mobile belts accreted during successive orogenic events [2]. These mobile belts are important source terrains for uranium because their constituent granites and migmatites carry elevated uranium concentrations of 4–10 ppm, compared with ~2.8 ppm for the average continental crust [10]. Phanerozoic sedimentary basins deposited over this basement, principally the Karoo Supergroup, constitute the principal uranium reservoir in Tanzania. The most recent contribution to the regional architecture is the EARS, which has been seismically active since the Oligocene–Miocene and continues to reactivate pre-existing basement faults [3], [4].

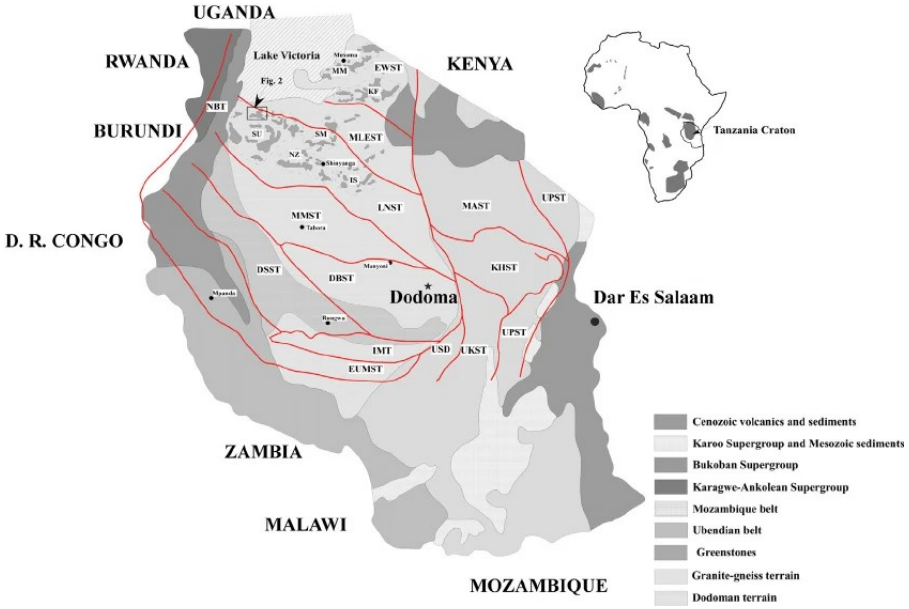


Figure 2 - Simplified geological map of Tanzania showing principal tectonic units and terrane boundaries, distribution of Precambrian basement units (Tanzania Craton, Ubendian Belt, Mozambique Belt, Kibaran Belt), Karoo sedimentary basins, and the East African Rift System

DOI: https://doi.org/10.60797/GEO.2026.9.1.2

Note: known uranium occurrences (Mkuju, Manyoni, Bahi) are marked with symbols. Modified after Kabete et al. (2012) [2] and the Geological Survey of Tanzania

 © Authors of the article / Authors of the article

2.2. The Karoo Supergroup and the Luwegu sub-basin

The Karoo Supergroup is the dominant uranium-hosting geological unit in southern Tanzania. Within Tanzania, Karoo sediments occur in three distinct sub-basins: the Ruhuhu Basin, the Luwegu sub-basin, and the Selous Basin (Fig. 3) [4]. The Luwegu sub-basin is an asymmetric NW–SE trending half-graben bounded in the south-west by a major normal fault and containing a near-complete Karoo succession reaching 3,000–4,000 m in the depocenter [5]. The uranium-hosting interval — informally called the Minjingu Formation — consists of upper Permian to lower Triassic medium-grained, cross-bedded feldspathic sandstones with high primary permeability that facilitated the migration of oxidizing groundwaters responsible for roll-front ore body development [5], [11]. The Mkuju River project, operated successively by Mantra Resources and Uranium One, defined a JORC-compliant inferred resource of 110.6 million pounds U_3O_8 at 547 ppm from this horizon [5].

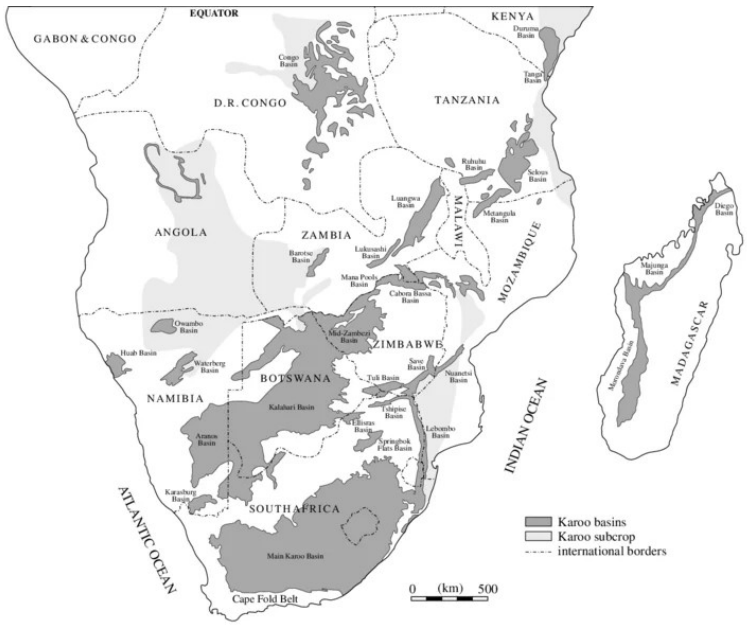


Figure 3 - Distribution of Karoo basins across south-central Africa showing the Ruhuhu, Luwegu, and Selous sub-basins in Tanzania; the NW–SE trending Luwegu sub-basin half-graben is the host of the Mkuju River uranium system
DOI: https://doi.org/10.60797/GEO.2026.9.1.3

Note: after Johnson et al. (1996) [4] and Kreuser et al. (1990)

2.3. Local geology of the Namayeni area

The Namayeni block is located in the Namtumbo District, Ruvuma Region, at approximately 10°25′S, 36°55′E. The terrain is the undulating Karoo plateau, ranging from 292 to 1,563 m above sea level. Climate is semi-arid tropical, with 900–1,100 mm annual rainfall concentrated in November–April. Four stratigraphic units are recognized from field mapping and historical drill-core logs (Fig. 4) [5], [11]:

Unit 1. Lower Reduced Sandstone: grey to dark-grey, medium- to coarse-grained feldspathic sandstones containing carbonized plant fossils and disseminated pyrite (FeS_2). The reducing capacity of organic matter and iron sulphides makes Unit 1 the principal ore-hosting horizon, where uranium precipitates at the redox boundary between advancing oxidizing groundwater and the reduced host rock.

Unit 2. Transitional / ore-bearing horizon: a laterally variable interval of 5–25 m thickness characterized by color mottling from grey to yellow-green, partial pyrite oxidation to goethite and jarosite, and secondary uranium mineral coatings visible as pale-yellow UV-fluorescent films. This horizon constitutes the roll-front proper and the primary exploration target at Namayeni.

Unit 3. Oxidized Sandstone: reddish-brown to orange-red, fine- to medium-grained sandstones in which pyrite has been fully replaced by hematite and goethite, and organic carbon has been oxidized. Uranium concentrations are generally below 20 ppm, representing material upgradient of the ore front from which uranium has been mobilized into solution.

Unit 4. Mudstone / Siltstone caprock: variable-thickness grey to brown mudstones and siltstones that form an aquitard restricting vertical migration of oxidizing groundwaters, thereby focusing mineralization within the underlying sandstone aquifer.

 © Authors of the article / Authors of the article

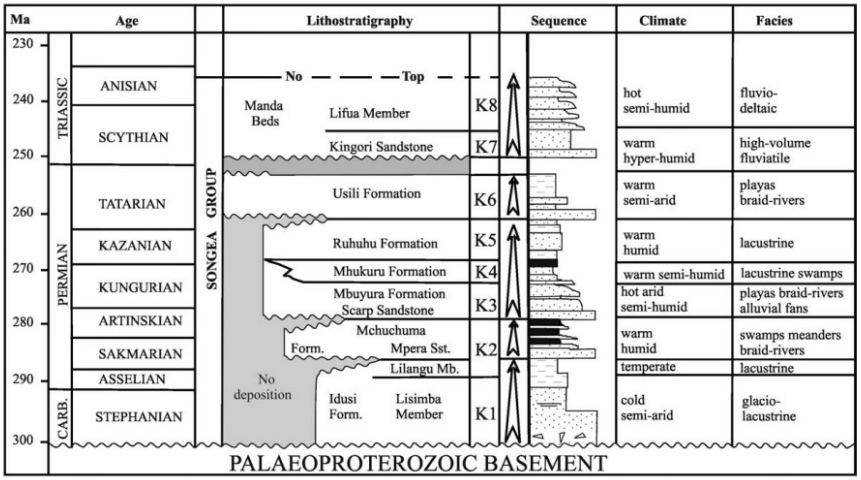


Figure 4 - Lithostratigraphy of the Karoo Supergroup in the Luwegu sub-basin, Tanzania, showing the four principal lithostratigraphic units, their depositional environments, and the position of the uranium-bearing horizon relative to the redox zonation

DOI: https://doi.org/10.60797/GEO.2026.9.1.4

Note: Unit 1: reduced sandstone; Unit 2: transitional ore horizon; Unit 3: oxidized sandstone; Unit 4: mudstone/siltstone caprock; after Diekmann and Wopfner (1996) [4], [11]

Two fault families govern the structural architecture of Namayeni: NW–SE normal faults (displacements 10–100 m) paralleling the Luwegu sub-basin bounding system, and ENE–WSW transfer faults related to Cenozoic EARS reactivation [3], [11]. Intersections of these two families create zones of maximum structural permeability that served as conduits for uranium-bearing oxidizing groundwaters during both the primary Mesozoic mineralization event and subsequent Cenozoic supergene oxidation.

Materials and Methods

3.1. Datasets

Five primary datasets were used in the analysis (see Table 1). Landsat 8 OLI Collection 2 Level-2 Surface Reflectance data for WRS-2 Path 165/Row 063 were obtained from the USGS EarthExplorer portal, with a dry-season cloud cover of less than 2% — well within the 10% maximum recommended for geological applications [12]. The SRTM 1 arc-second Global DEM was obtained from the NASA LP DAAC archive. All processing was performed in QGIS 3.34 LTR with the GDAL and SAGA analytical libraries [13].

Table 1 - Primary datasets used in the remote sensing and structural analysis

DOI: https://doi.org/10.60797/GEO.2026.9.1.5

Dataset	Specification	Source	Application
Landsat 8 OLI Collection 2 Level-2	Path 165/Row 063; 30 m; dry-season acquisition	USGS EarthExplorer	IOI, CMI, CBI, NDVI; FCCs; IUPI
SRTM DEM 1 Arc-Second Global	~30 m; elevation 292–1,563 m	NASA LP DAAC / USGS	Hillshade, slope, aspect, lineaments, lineament density
GST Geological Maps	1:250,000–1:50,000	Geological Survey of Tanzania; Mantra Resources (2011)	Lithological context; lineament reference
Google Satellite Hybrid	~0.5 m (variable)	QGIS QuickMapServices	Visual basemap for map layouts
QGIS 3.34 LTR	Open-source GIS (GDAL/SAGA)	qgis.org	All preprocessing, raster calculation, structural analysis, cartography

3.2. Image pre-processing

We converted Landsat Collection 2 Level-2 integer band values to fractional surface reflectance (0.0–1.0) by applying the USGS scaling factor of 0.0000275 and additive offset of −0.2 via the Semi-Automatic Classification Plugin (SCP v. 7.10.3) in QGIS [12]. Cloud pixels and cloud shadows were masked using the QA_PIXEL quality assessment band — a largely

 © Authors of the article / Authors of the article

mechanical step given the very low cloud cover of the selected scene. We then derived a vegetation mask from the NDVI: NDVI = (B5 − B4) / (B5 + B4).

We excluded all pixels with NDVI ≥ 0.30 from subsequent spectral index calculations. The 0.30 cut-off was not chosen arbitrarily: inspecting the NDVI frequency histogram showed a clear inflection between the soil-dominated peak and the vegetated tail, and 0.30 sat squarely at that break — a criterion consistent with standard practice for geological remote sensing in eastern African dry-season imagery [7], [14]. In practice, almost nothing was masked out, which itself turned out to be a useful finding.

3.3. Spectral index calculation

We computed three band-ratio indices in the QGIS Raster Calculator. Each targets a distinct mineralogical signal relevant to uranium roll-front exploration:

Iron Oxide Index (IOI = B6/B5, SWIR-1/NIR): exploits the strong reflectance of ferric iron minerals (hematite, goethite, jarosite) in SWIR-1 relative to NIR. Elevated IOI values identify the oxidised zone upgradient of the roll-front, where pyrite and ferrous iron-bearing minerals have been converted to iron oxides by incoming oxygenated groundwater [6], [7].

Clay Minerals Index (CMI = B6/B7, SWIR-1/SWIR-2): exploits hydroxyl absorption features of kaolinite (~2.20 μm) and illite (~2.22 μm) in the SWIR-2 band. High CMI values identify clay-enriched alteration haloes in the redox transition zone immediately surrounding the ore body [7], [8].

Carbonate Band Index (CBI = B7/B6, SWIR-2/SWIR-1): detects the CO_3 stretching absorption at ~2.35 μm in SWIR-2. In the semi-arid Namayeni environment, elevated CBI indicates calcrete accumulations and diagenetic carbonate cements [15].

Each index raster was normalized to a 0–1 range prior to integration.

3.4. Structural analysis

We generated three hillshade images from the SRTM DEM at solar azimuths of 45°, 135°, and 315° with a fixed solar altitude of 30° using the QGIS GDAL Hillshade algorithm, then composited them into a single RGB image (R = 45°, G = 135°, B = 315°). This multi-azimuth approach was deliberate — it renders linear topographic features visible regardless of their orientation, so no fault family gets preferentially suppressed by a single illumination direction [9]. Lineaments were then traced by hand as vector features wherever a continuous linear expression — a ridge crest, straight valley axis, escarpment edge, or sharp hillshade color boundary — extended for at least 500 m. Short, ambiguous features below that length were left undigitized. Orientations and lengths were extracted automatically via the QGIS Field Calculator, and we built a lineament density surface by kernel density estimation using a 5 km search radius, which was then normalised to 0–1.

3.5. Integrated Uranium Prospectivity Index (IUPI)

We combined the four normalised layers by weighted linear combination in the QGIS Raster Calculator:

$$IUPI = (0.35 \times IOI_norm) + (0.30 \times CMI_norm) + (0.20 \times CBI_norm) + (0.15 \times LineDens_norm)$$

Weight allocation followed the framework of Bonham-Carter [16] and Carranza [17], grounded in how directly each layer points to roll-front mineralization. IOI takes the highest share (0.35) because iron oxide enrichment is the most immediate spectral expression of the oxidized zone. We gave CMI 0.30, reflecting that clay alteration halos, while slightly more distal, are a reliable and well-documented indicator [7], [8]. CBI received 0.20 as useful supporting context rather than a primary target criterion — carbonate anomalies in semi-arid settings carry more ambiguity than the other indices. Lineament density was kept at 0.15; structural control matters for ore body localization, but we did not want a single high-density fault intersection to override a weak spectral signal. Finally, two prospectivity tiers were read off the IUPI histogram: Tier 1 (IUPI ≥ 0.65, highest confidence) and Tier 2 (IUPI 0.45–0.64, elevated confidence).

3.6. Uranium mineralogy

Representative rock samples from historical drill-core archives of the Namayeni area were examined in reflected light, followed by SEM-EDS backscattered electron imaging to identify uranium mineral phases and their textural relationships with host minerals. EPMA was applied to quantify the major-element composition of uraninite and coffinite, from which chemical U–Pb ages were estimated using measured PbO contents. XRD was used to confirm secondary uranium mineral identification through characteristic d-spacing values.

Main results

4.1. NDVI and vegetation mask

The NDVI map (Fig. 5) spans −0.435 to 1.0, reflecting the full range of surface types from dry sandy streambeds to dense riparian woodland. However, the binary vegetation mask (NDVI threshold 0.30) reveals that virtually all of the study area returns a value below the threshold during the dry-season acquisition. Only the narrow riparian corridors following the Mkuju River and its principal tributaries, together with small patches on the eastern escarpment, carry a photosynthetic signal sufficient to be excluded. This near-total bare-ground environment, covering more than 97% of the scene, is a prerequisite for reliable geological remote sensing: the reflected SWIR and visible spectra derive from bare soil and exposed rock surfaces rather than leaf chemistry, confirming that the IOI, CMI, and CBI maps constitute valid mineralogical surface signatures across almost the entire study area.

 © Authors of the article / Authors of the article

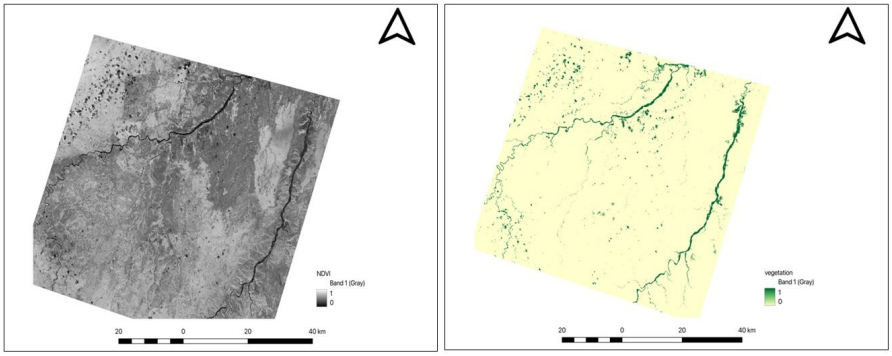


Figure 5 - On the left side NDVI greyscale map (NDVI = (B5−B4)/(B5+B4)). Dark = low NDVI (bare ground); bright = high NDVI (vegetation). On the right-side Binary vegetation mask (pale yellow = NDVI < 0.30, retained for analysis; dark green = NDVI ≥ 0.30, excluded). Less than 3% of the scene is masked Scale bar = 40 km. WGS 84 / UTM Zone 36S
DOI: https://doi.org/10.60797/GEO.2026.9.1.6

4.2. False color composites

Four false color composites were generated to provide an overview of surface spectral properties prior to quantitative index analysis. The FCC_IOI composite (Fig. 6) highlights the eastern and north-central sectors in magenta-crimson tones, indicating strong Fe^{3+} reflectance from surface-exposed oxidized Karoo sandstones of Unit 3 [6]. The FCC_CMI composite (Fig. 7) shows blue-lavender tones extending broadly across the central and southern portions of the scene, with the clay-enriched domain clearly offset southward and westward of the iron oxide zone — a spatial separation that is geologically meaningful because it mirrors the expected downgradient displacement of the clay alteration transition zone in roll-front systems [7], [8]. The FCC_CBI composite (Fig. 8) is dominated by teal-green tones consistent with landscape-wide carbonate content in semi-arid soils, with the strongest signal concentrated along valley floors. The FCC_NDVI composite (Fig. 9) confirms the preponderance of bare ground and validates the geological interpretability of the other three composites.

 © Authors of the article / Authors of the article

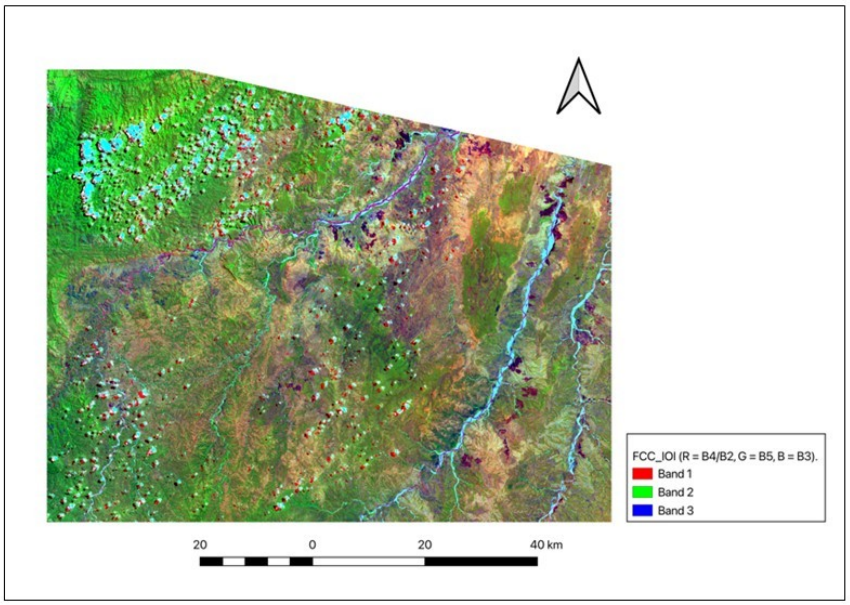


Figure 6 - FCC_IOI false color composite (R = B4/B2, G = B5, B = B3)
DOI: https://doi.org/10.60797/GEO.2026.9.1.7

Note: magenta-crimson tones indicate elevated Fe^{3+} spectral response; green = riparian vegetation; white = high-reflectance surfaces. Scale bar = 40 km; WGS 84 / UTM Zone 36S

 © Authors of the article / Authors of the article

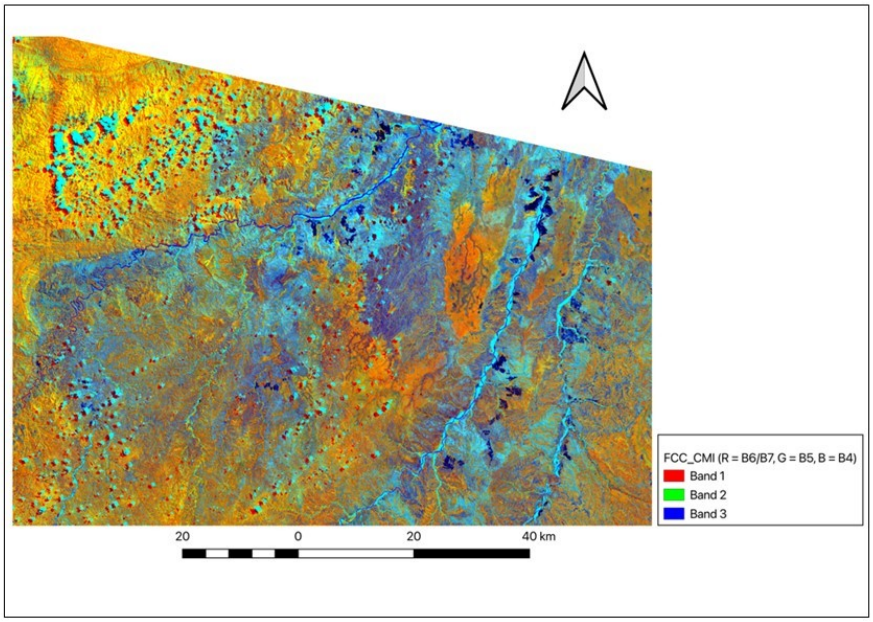


Figure 7 - FCC_CMI false color composite (R = B6/B7, G = B5, B = B4)
DOI: https://doi.org/10.60797/GEO.2026.9.1.8

Note: blue-lavender tones indicate elevated CMI corresponding to clay mineral enrichment (kaolinite, illite); scale bar = 40 km; WGS 84 / UTM Zone 36S

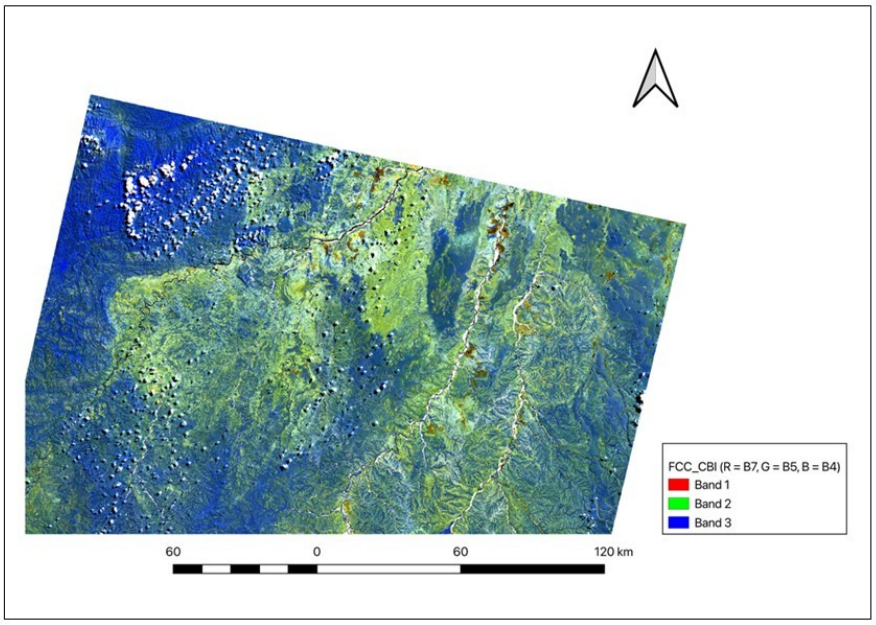


Figure 8 - FCC_CBI false color composite (R = B7, G = B5, B = B4). Teal-green tones indicate elevated carbonate spectral response; strongest signal is concentrated along drainage corridors. Scale bar = 120 km. WGS 84 / UTM Zone 36S
DOI: https://doi.org/10.60797/GEO.2026.9.1.9

 © Authors of the article / Authors of the article

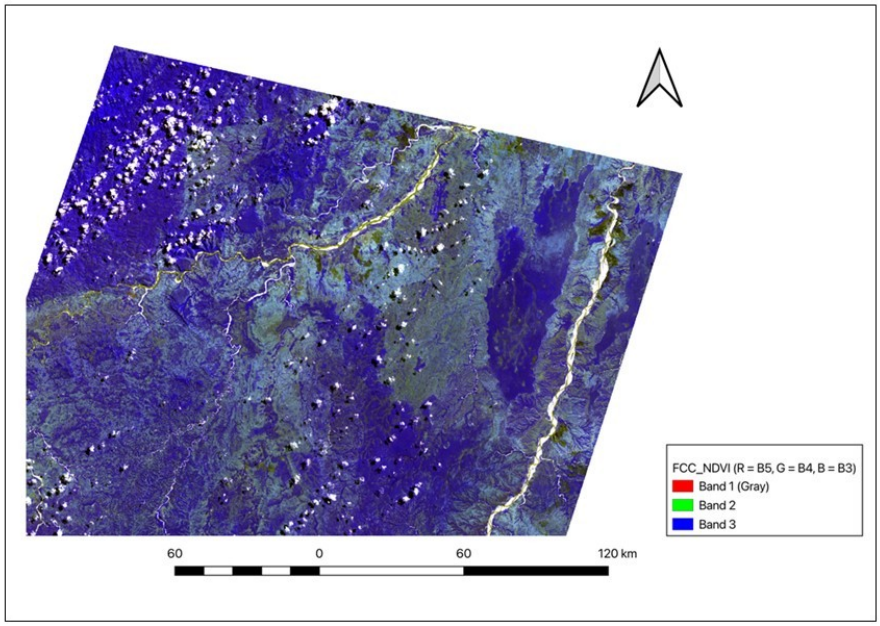


Figure 9 - FCC_NDVI false color composite
DOI: https://doi.org/10.60797/GEO.2026.9.1.10

Note: deep blue tones confirm near-total bare-ground cover during dry-season acquisition; yellow marks active riparian vegetation; scale bar = 40 km; WGS 84 / UTM Zone 36S

4.3. Iron Oxide Index (IOI)

The IOI map (Fig. 10) defines five discrete anomaly zones (IO-1 to IO-5) with values between 1.0 and 1.7 against a regional background of approximately 1.1–1.2. The segmented spatial pattern of these zones — rather than a single continuous front — indicates that the paleo-oxidation front is structurally compartmentalized, most probably by permeability contrasts between fluvial channel sandstone bodies and interfluve mudstones, or by fault-controlled aquifer displacement [6], [10]. In roll-front uranium systems, the oxidized zone develops upgradient of the ore body as pyrite and ferrous iron-bearing minerals react with oxygenated groundwater to precipitate goethite and hematite; the IOI is thus the most direct remote sensing indicator of the lateral position of the oxidized limb of the roll-front [6], [7]. The five IOI anomalies define the spatial distribution of this limb across the Namayeni block and provide the primary target vectors for ground follow-up.

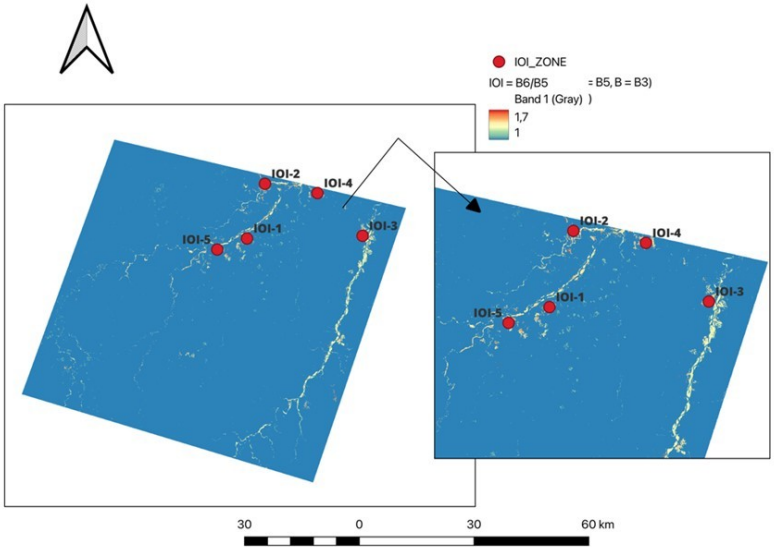


Figure 10 - Iron Oxide Index (IOI = B6/B5) map. Five anomaly zones IO-1 to IO-5 are labelled. IOI values 1.0–1.7 (warm = high). Scale bar = 60 km. WGS 84 / UTM Zone 36S
DOI: https://doi.org/10.60797/GEO.2026.9.1.11

4.4. *Clay Minerals Index (CMI)*

 © Authors of the article / Authors of the article

Three CMI anomaly zones (CA-1, CA-2, CA-3; values 0.8–1.5) were delineated (Fig. 11). The CMI anomaly domain extends considerably further southward and westward than the IOI domain — the anticipated downgradient direction for the transition zone of the roll-front [7], [8]. In this zone, acidic oxidizing groundwaters hydrolyze feldspars and aluminosilicate minerals to produce kaolinite and illite, the phases responsible for the elevated SWIR-1/SWIR-2 ratio captured by the CMI [8]. The coincidence of zones CA-2 and CA-3 with structural lineament clusters further supports the interpretation that clay alteration was channeled along fault-controlled permeability pathways [11], [18].

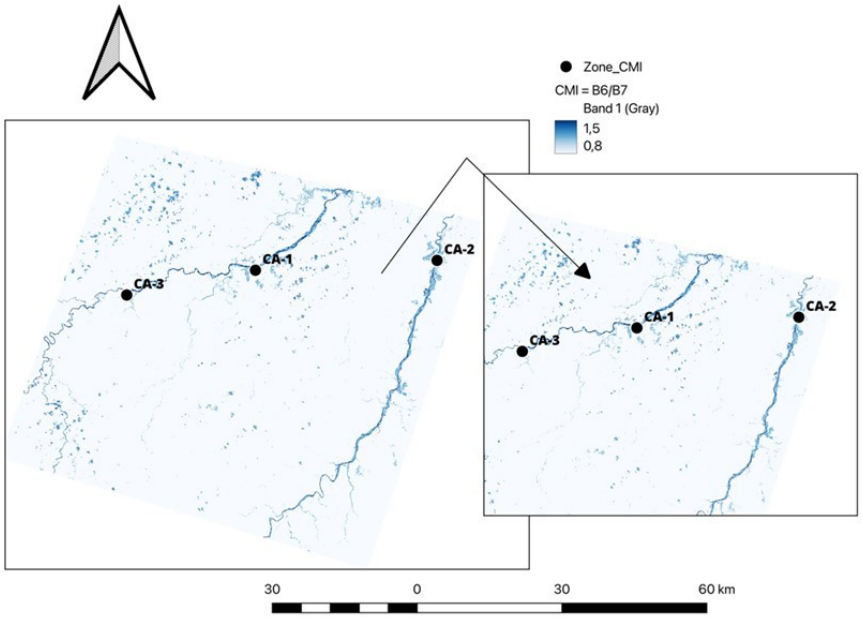


Figure 11 - Clay Minerals Index (CMI = B6/B7) map
DOI: https://doi.org/10.60797/GEO.2026.9.1.12

Note: three anomaly zones CA-1 to CA-3 are labelled; CMI values 0.8–1.5 (dark blue = high); scale bar = 60 km; WGS 84 / UTM Zone 36S

4.5. Carbonate Band Index (CBI)

Three CBI anomaly zones (CB-1, CB-2, CB-3; values 0.6–1.2) were identified (Fig. 12). Zone CB-1 is sub-circular and likely reflects a localized carbonate-cemented sandstone body, possibly a diagenetically modified Karoo channel deposit. Zones CB-2 and CB-3 display elongated, branching geometries aligned with drainage corridors and structural lineaments, indicating that carbonate accumulation was controlled by groundwater flow along permeable fracture pathways [15]. In the semi-arid Namayeni environment (900–1,100 mm annual rainfall), CBI anomalies may reflect diagenetic calcite cement, pedogenic calcrete, or redox-boundary carbonate precipitation; their exploration significance therefore increases considerably when they overlap spatially with IOI and CMI anomalies [15], [16].

 © Authors of the article / Authors of the article

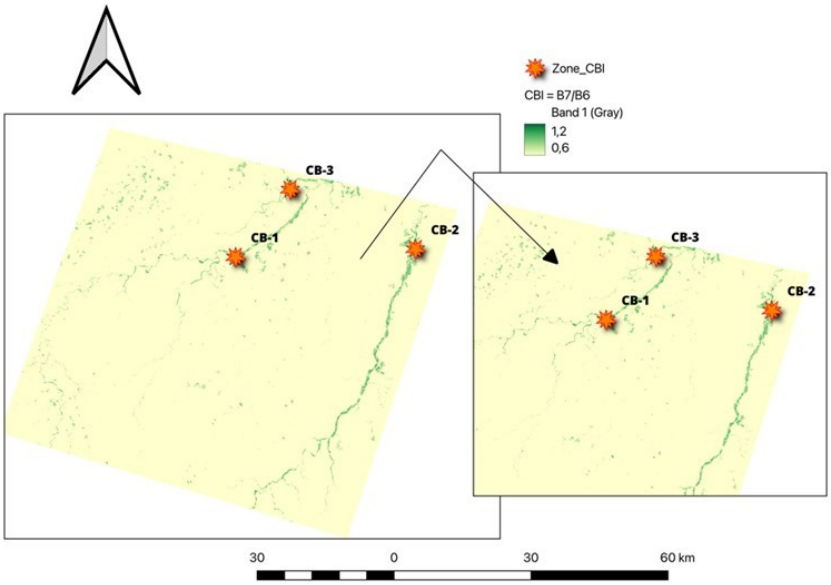


Figure 12 - Carbonate Band Index (CBI = B7/B6) map
DOI: https://doi.org/10.60797/GEO.2026.9.1.13

Note: three anomaly zones CB-1 to CB-3 are labelled; CBI values 0.6–1.2 (dark green = high); scale bar = 60 km; WGS 84 / UTM Zone 36S

4.6. Multi-azimuth hillshade composite and structural lineament mapping

The multi-azimuth hillshade RGB composite (Fig. 13) reveals a highly ordered structural fabric across the study area. The north-western quadrant exhibits a dense network of closely incised valleys producing a coarse texture, while the central and south-eastern portions show progressively broader valley forms. Manually digitized lineaments (red lines) are aligned in both the NW–SE and ENE–WSW directions, consistently tracking linear valley axes and sharp hillshade color transitions — characteristics that are diagnostic of fault-controlled topographic incision [9].

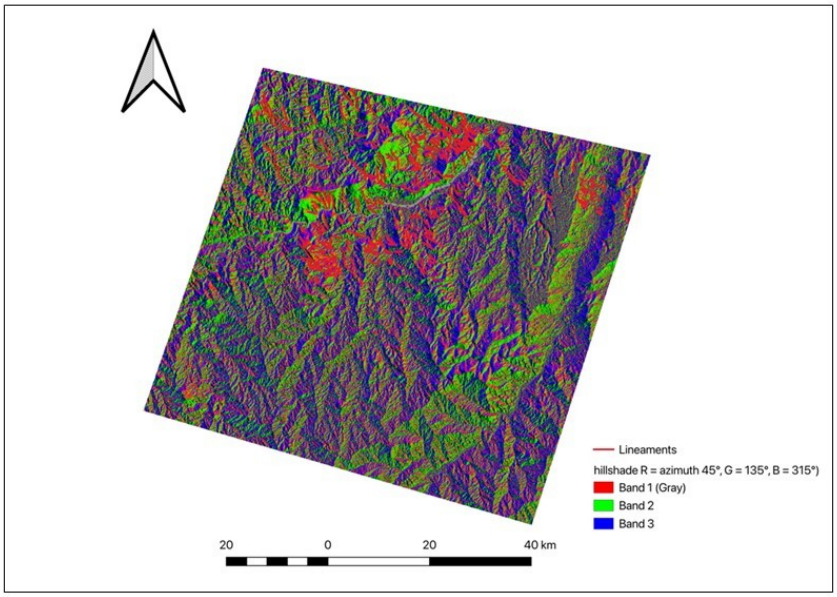


Figure 13 - Multi-azimuth hillshade RGB composite (R = azimuth 45°, G = 135°, B = 315°; solar altitude 30°) with digitized structural lineaments (*red lines*)
DOI: https://doi.org/10.60797/GEO.2026.9.1.14

Note: scale bar = 40 km; WGS 84 / UTM Zone 36S

The integrated structural map with rose diagram (Fig. 14) confirms a bimodal lineament fabric: a dominant NW–SE family centred at ~316°, corresponding to Luwegu sub-basin bounding faults, and a secondary NE–SW family at 045–060°, interpreted as transfer faults related to Cenozoic EARS extension [3], [4]. The association of lineaments with slope-break

 © Authors of the article / Authors of the article

zones (Fig. 16) and systematic azimuthal transitions on the aspect map (Fig. 15) provides independent physical validation that the digitized lineaments represent tectonic structures rather than data artefacts [9], [19].

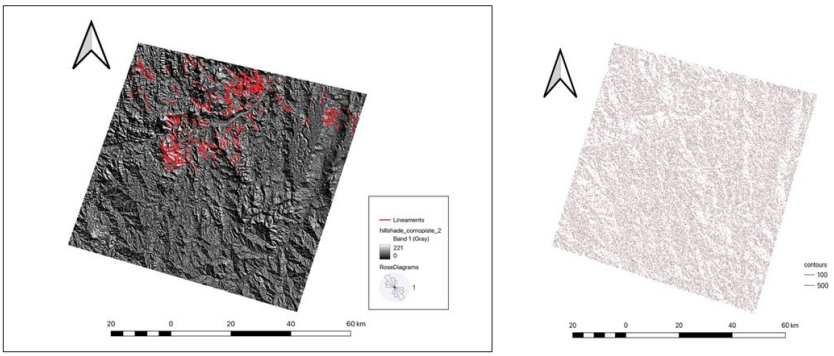


Figure 14 - Integrated structural and lineament map on greyscale hillshade background with DEM elevation ramp
DOI: https://doi.org/10.60797/GEO.2026.9.1.15

Note: red lines = digitized lineaments; rose diagram (inset) shows dominant NW–SE mode (~316°) and secondary NE–SW family; Scale bar = 60 km; WGS 84 / UTM Zone 36S

4.7. Terrain analysis — DEM, slope, and aspect

The clipped SRTM DEM (Fig. 15) shows that the study area ranges from 292 m in the south-east to 1,563 m in the north-west. A dissected plateau in the north-west hosts the highest elevations; elevations decrease progressively to the south and east, with lower terrain concentrated along principal drainage channels. The drainage pattern is strongly dendritic, indicating erosion within a geologically homogeneous sandstone terrain with structurally guided preferential incision.

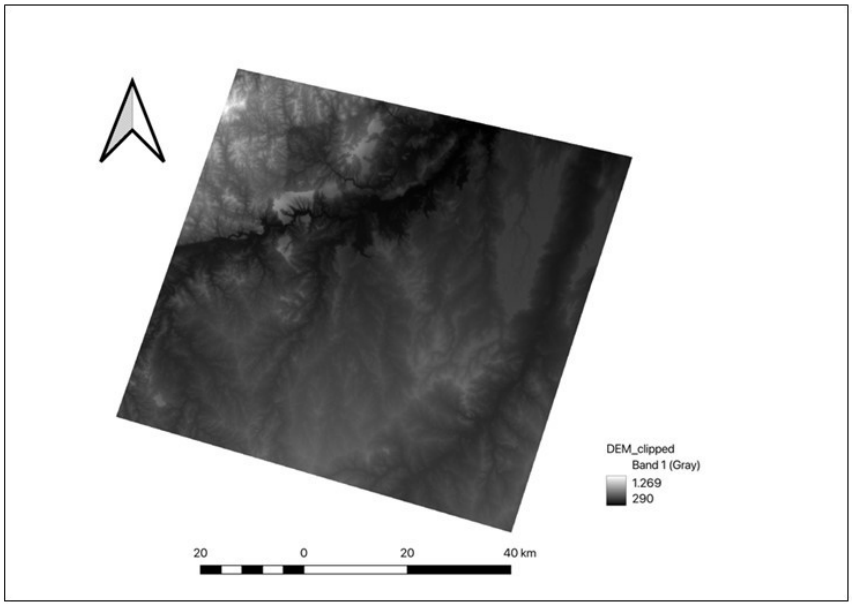


Figure 15 - Clipped SRTM 1 arc-second DEM of the Namayeni study area
DOI: https://doi.org/10.60797/GEO.2026.9.1.16

Note: bright = high elevation (max 1,563 m); dark = low elevation (min 290 m); dendritic drainage network clearly visible; scale bar = 40 km; WGS 84 / UTM Zone 36S

The slope map (Fig. 17) confirms that digitized lineaments are systematically co-located with the steepest terrain gradients, represented by the brightest pixels. This spatial association validates the tectonic authenticity of the lineament dataset: fault-related escarpments and structurally guided valley incisions produce the high-gradient zones captured by the SRTM-derived slope raster [9], [19].

 © Authors of the article / Authors of the article

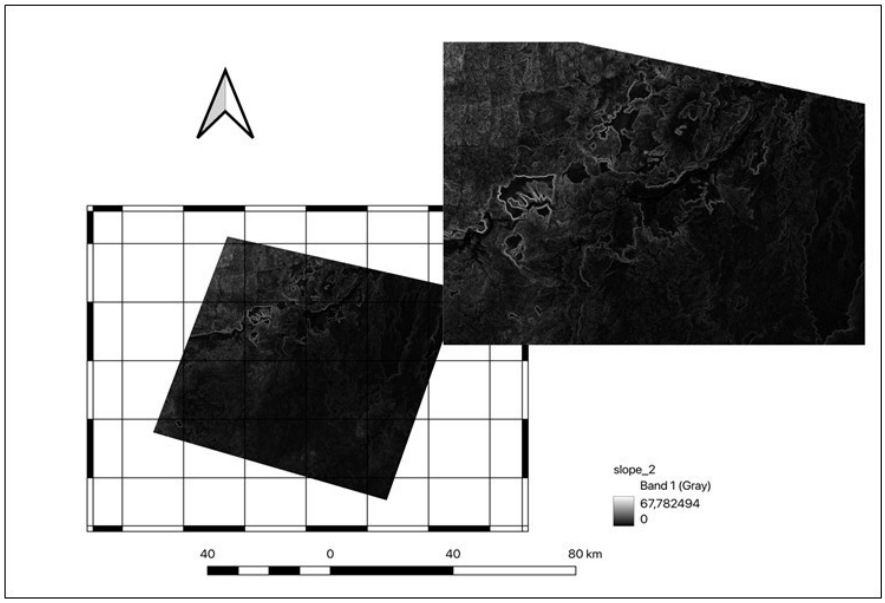


Figure 16 - Slope map (SRTM DEM; values 0°–67.8)
DOI: https://doi.org/10.60797/GEO.2026.9.1.17

Note: bright = steep slopes; lineaments are spatially associated with slope-break zones, confirming structural topographic control; scale bar = 80 km; WGS 84 / UTM Zone 36S

The aspect map (Fig. 17) provides a second independent validation. Each digitized lineament corresponds to a systematic transition in the downslope azimuth direction — a characteristic of fault-controlled escarpments and structurally guided valley axes rather than gradual hillslope transitions [9]. The bimodal NW–SE and NE–SW structural pattern is clearly visible on the aspect map as intersecting families of differently oriented directional boundaries.

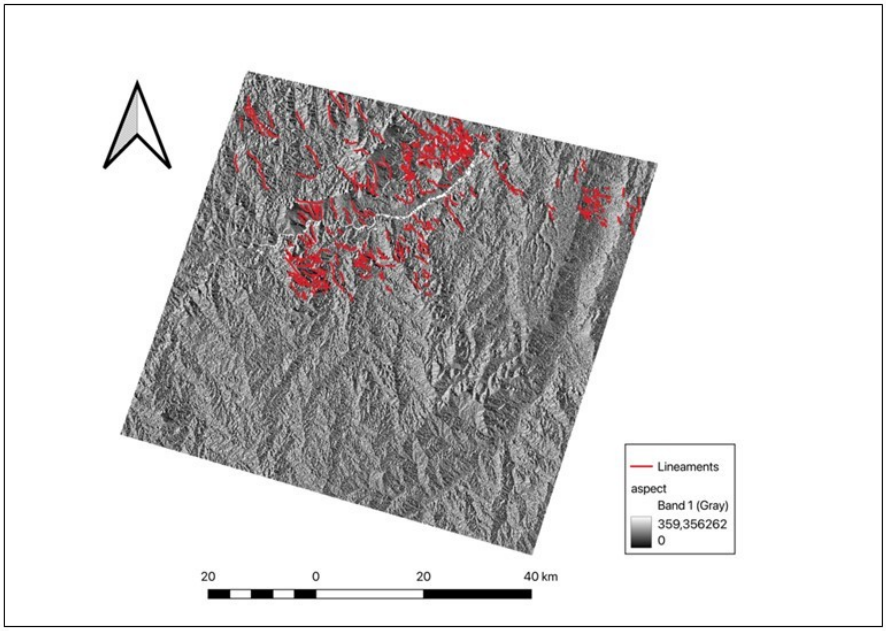


Figure 17 - Aspect map (SRTM DEM; values 0°–360°) with digitized lineaments overlaid (*red lines*)
DOI: https://doi.org/10.60797/GEO.2026.9.1.18

Note: greyscale encodes downslope azimuth; each lineament marks a systematic aspect transition consistent with fault-controlled terrain; scale bar = 40 km; WGS 84 / UTM Zone 36S

4.8. Lineament density

The lineament density surface (Fig. 18) reveals 15–20 discrete circular nodes with maximum density values reaching 0.00933, concentrated in the north-central sector of the study area. These nodes correspond to intersection points of NW–SE and NE–SW lineament families. Fault intersections create localized increases in secondary porosity and permeability that are

 © Authors of the article / Authors of the article

widely recognized as preferred sites for uranium ore body development in sandstone-hosted deposits: they simultaneously allow deep penetration of oxidizing groundwater and provide structural barriers that promote precipitation of uranium at redox boundaries [10], [16].

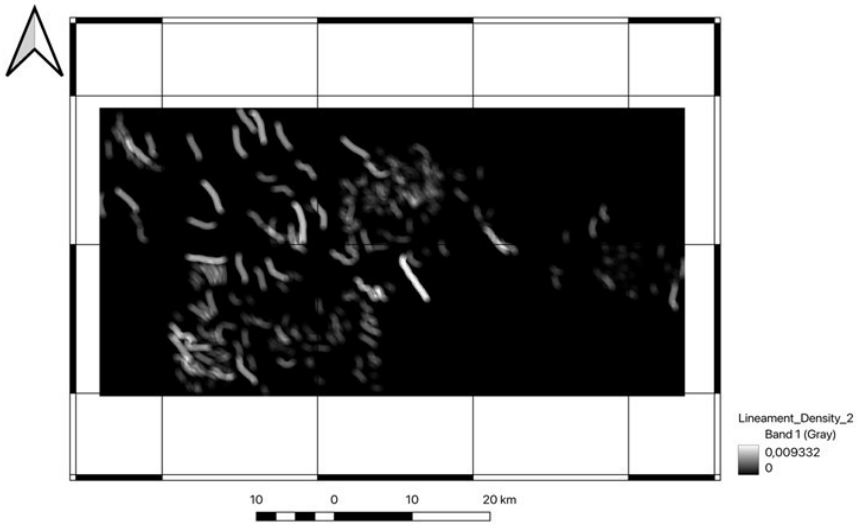


Figure 18 - Lineament density heatmap (kernel density estimation; 5 km search radius; length-weighted)
DOI: https://doi.org/10.60797/GEO.2026.9.1.19

Note: bright = high density (max 0.009332); dark = low density (0); approximately 15–20 discrete high-density nodes are visible in the north-central sector; scale bar = 20 km; WGS 84 / UTM Zone 36S

4.9. Integrated Uranium Prospectivity Index (IUPI)

The IUPI raster (Fig. 19) reaches a maximum value of 0.611, identifying two Tier-2 priority zones (IUPI ≥ 0.45) in the north-central sector. No pixel exceeded the Tier-1 threshold of 0.65, indicating that the four criteria do not achieve maximum simultaneous expression at the 30 m Landsat resolution within the present dataset. Nevertheless, the two Tier-2 zones represent the geologically most significant exploration targets identified in this study because they exhibit the highest co-occurrence of IOI > 1.40, CMI > 1.15, CBI anomaly, and high lineament density at lineament intersection nodes.

The NW–SE elongation of the IUPI anomaly pattern mirrors the orientation of the dominant structural lineaments and the inferred direction of paleo-groundwater flow within the Luwegu sub-basin aquifer. Roll-front ore bodies in the Mkuju River province are expected to develop as crescent-shaped bodies perpendicular to groundwater flow, with long axes parallel to the redox boundary [5], [11]. The elongated IUPI pattern is therefore geometrically consistent with this ore body model, suggesting that the Tier-2 zones occupy sections of the paleo-redox boundary where structural permeability and spectral anomaly intensity are simultaneously highest.

The Namayeni IUPI results compare favorably with remote sensing prospectivity studies from analogous sandstone-hosted uranium systems. In the Chu-Sarysu Basin of Kazakhstan, Landsat-derived iron oxide and clay mineral indices successfully delineated the oxidized margins of economic roll-front deposits [20]. In the Colorado Plateau of the United States, ASTER and Landsat spectral analysis mapped iron oxide zones indicative of roll-front oxidized limbs [21]. The geologically closest analogue is the Kayelekera uranium deposit in Malawi, hosted in Karoo-equivalent sandstones with the same NW–SE structural fabric and uranium mineralogy [22].

 © Authors of the article / Authors of the article

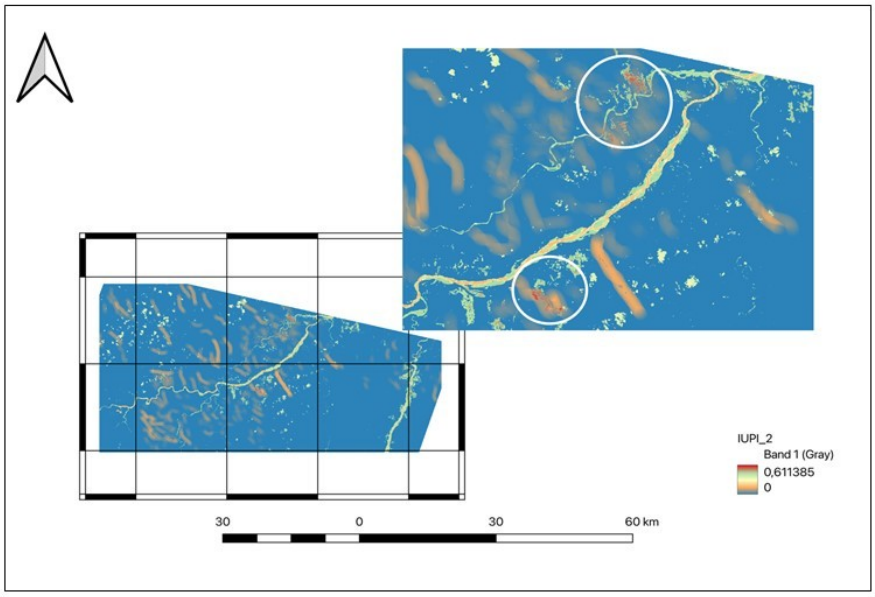


Figure 19 - Integrated Uranium Prospectivity Index (IUPI) map
DOI: https://doi.org/10.60797/GEO.2026.9.1.20

Note: IUPI raster: 0 (blue) to 0.611 (deep red); orange outlines = Tier-2 anomaly zones (IUPI ≥ 0.45); white circles on inset = the two highest-value target zones; IUPI = (0.35×IOI_norm) + (0.30×CMI_norm) + (0.20×CBI_norm) + (0.15×LineDens_norm); scale bar = 60 km; WGS 84 / UTM Zone 36S

4.10. Uranium mineralogy

Primary uranium mineralization at Namayeni is dominated by two phases. Uraninite (UO_{2+x}, x = 0–0.25) occurs in three textural settings:

1) very fine-grained (1–20 μm) disseminations coating detrital quartz and feldspar grain surfaces within the ore-zone sandstone;

2) colloform to botryoidal aggregates filling intergranular pores;

3) rare euhedral to subhedral crystals (5–50 μm) enclosed within authigenic clay mineral aggregates.

EPMA analysis yields UO_2 contents of 82.1–89.6 wt%, ThO_2 consistently below 0.5 wt% — confirming a diagenetic rather than magmatic or hydrothermal origin — and PbO contents of 0.8–2.3 wt%, corresponding to calculated chemical ages of 200–290 Ma (Permian–Triassic). These ages are consistent with syndiagenetic precipitation during early Mesozoic burial of the Karoo succession [23].

Coffinite ($USiO_4 \cdot nH_2O$) is the second most abundant primary phase, occurring principally as pseudomorphs after detrital heavy minerals (zircon, monazite) and as fine-grained aggregates intergrown with authigenic clays. EDS analysis yields SiO_2 contents of 14.2–16.8 wt%, near-stoichiometric for $USiO_4$. Coffinite is more prevalent in reduced-zone samples below the redox boundary, consistent with its thermodynamic stability under lower uranium activities and higher silica activities compared with uraninite [23].

Secondary uranium minerals formed through supergene oxidation of primary phases include four assemblages. Carnotite ($K_2(UO_2)_2(VO_4)_2 \cdot 3H_2O$) is the most abundant, forming bright yellow-green powdery coatings on fracture surfaces; its identification was confirmed by XRD using characteristic d-spacings at 5.18 Å, 4.87 Å, and 3.35 Å [24]. Tyuyamunite ($Ca(UO_2)_2(VO_4)_2 \cdot 5–8H_2O$) co-occurs with carnotite and is distinguished by a calcium-dominant EDS signature, with the carnotite/tyuyamunite ratio controlled by local K/Ca ratios in porewater. Autunite ($Ca(UO_2)_2(PO_4)_2 \cdot 10–12H_2O$) occurs as subordinate pale greenish-yellow UV-fluorescent crystals in near-surface weathered samples, precipitated where phosphate was available from dissolution of detrital apatite. Schoepite ($((UO_2)_4O(OH)_6 \cdot 6H_2O$) was identified as fine-grained yellowish coatings in the most heavily oxidized samples, consistent with its role as an early supergene oxide product of uraninite [24], [25].

This mineral paragenesis — primary uraninite and coffinite followed by supergene carnotite, tyuyamunite, autunite, and schoepite — records a two-stage history: (i) primary roll-front precipitation during Mesozoic diagenesis (200–290 Ma); and (ii) Cenozoic supergene reworking following EARS-related uplift and enhanced meteoric groundwater infiltration. This paragenesis is identical to that documented at the Mkuju River deposit [5] and closely comparable to Kayelekera [22], confirming that Namayeni is a segment of the same regional uranium system within the Luwegu sub-basin.

Conclusion

This study provides the first integrated remote sensing and mineralogical assessment of the Namayeni exploration block within the Mkuju River uranium province, Tanzania. Landsat 8 OLI spectral index analysis delineated five iron oxide anomaly zones, three clay alteration zones, and three carbonate anomaly zones whose spatial arrangement mirrors the redox zonation expected of sandstone-hosted roll-front uranium deposits: iron oxide enrichment upgradient in the oxidized zone, clay alteration in the transition zone, and carbonate precipitation along geochemical boundaries. Structural lineament analysis

 © Authors of the article / Authors of the article

confirmed a bimodal NW–SE and NE–SW fault network with 15–20 high-density intersection nodes concentrated in the north-central sector. Integration of all four normalized prospectivity layers into the IUPI defined two Tier-2 priority zones (IUPI up to 0.611) where all criteria simultaneously achieve their highest combined expression.

Uranium mineralogy — uraninite, coffinite, carnotite, tyuyamunite, autunite, and schoepite — is identical to the Mkuju River deposit and closely analogous to the Kayelekera deposit in Malawi, the nearest geological equivalent. EPMA-derived chemical ages of 200–290 Ma for uraninite confirm syndiagenetic Mesozoic mineralization, with Cenozoic supergene reworking recorded by the secondary mineral assemblage.

These findings establish a scientific basis for prioritizing field follow-up at Namayeni. Recommended next steps are: systematic rock chip and auger sampling over the two Tier-2 IUPI zones; thin section, XRD, SEM, and EPMA analysis of anomalous material; portable XRF geochemistry to map uranium and pathfinder element (V, Mo, Se, As) distributions; and integration with high-resolution Sentinel-2 or WorldView imagery to sharpen alteration boundaries below the 30 m Landsat resolution. The remote sensing methodology presented here — spectral index computation, structural lineament mapping, and IUPI synthesis in open-source QGIS, using freely available satellite data — is computationally efficient and directly transferable to other underexplored Karoo-type sedimentary basins across eastern and southern Africa.

Благодарности

Исследование выполнено при поддержке Программы стратегического академического лидерства РУДН. Авторы выражают искреннюю благодарность профессору А.Е. Котельникову, заведующему кафедрой недропользования и нефтегазового дела Инженерной академии РУДН, за научное руководство, а также консультанту г-ну Мохаммеду Ибрагиму. Данные спутников Landsat 8 OLI и цифровая модель рельефа SRTM DEM получены на безвозмездной основе из систем USGS EarthExplorer и NASA LP DAAC соответственно. Все операции пространственного анализа и картографирования выполнены с использованием свободно распространяемого программного обеспечения QGIS 3.34 LTR (QGIS Development Team, 2024).

Acknowledgement

This paper has been supported by the RUDN University Strategic Academic Leadership Program. The authors express sincere gratitude to Prof. Alexander Kotelnikov, Head of the Department of Mineral Development and Oil & Gas Engineering, RUDN University, for academic supervision, and to their consultant Mr. Mohammed Ibrahim. Landsat 8 OLI and SRTM DEM data were obtained at no cost from USGS EarthExplorer and NASA LP DAAC respectively. All spatial analysis and cartography used open-source QGIS 3.34 LTR (QGIS Development Team, 2024).

Конфликт интересов

Не указан.

Conflict of Interest

None declared.

Рецензия

Все статьи проходят рецензирование. Но рецензент или автор статьи предпочли не публиковать рецензию к этой статье в открытом доступе. Рецензия может быть предоставлена компетентным органам по запросу.

Review

All articles are peer-reviewed. But the reviewer or the author of the article chose not to publish a review of this article in the public domain. The review can be provided to the competent authorities upon request.

Список литературы на английском языке / References in English

1. Uranium 2022: Resources, Production and Demand : (the "Red Book") / Nuclear Energy Agency, International Atomic Energy Agency. — Paris: OECD Publishing, 2023. — 460 p.

2. Möller A. Crustal age domains and the evolution of the continental crust in the Mozambique Belt of Tanzania: combined Sm–Nd, Rb–Sr, and Pb–Pb isotopic evidence / A. Möller, K. Mezger, V. Schenk // Journal of Petrology. — 1998. — Vol. 39, № 5. — P. 749–783.

3. Chorowicz J. The East African rift system / J. Chorowicz // Journal of African Earth Sciences. — 2005. — Vol. 43, № 1–3. — P. 379–410. — DOI: 10.1016/j.jafrearsci.2005.07.019.

4. Kreuser T. Depositional evolution of Permo-Triassic Karoo basins in Tanzania with reference to their economic potential / T. Kreuser, H. Wopfner, C.Z. Kaaya [et al.] // Journal of African Earth Sciences. — 1990. — Vol. 10, № 1–2. — P. 151–167. — DOI: 10.1016/0899-5362(90)90052-G.

5. Uranium One Inc. Mkuju River Project : Updated Resource Estimate : Technical Report NI 43-101 / Uranium One Inc. — Toronto, 2012.

6. Dahlkamp F.J. Uranium Ore Deposits / F.J. Dahlkamp. — Berlin: Springer, 1993. — 460 p. — DOI: 10.1007/978-3-662-02892-6.

7. Sabins F.F. Remote sensing for mineral exploration / F.F. Sabins // Ore Geology Reviews. — 1999. — Vol. 14, № 3–4. — P. 157–183. — DOI: 10.1016/S0169-1368(99)00007-4.

8. Carranza E.J.M. Mineral imaging with Landsat Thematic Mapper data for hydrothermal alteration mapping in heavily vegetated terrane / E.J.M. Carranza, M. Hale // International Journal of Remote Sensing. — 2002. — Vol. 23, № 22. — P. 4827–4852.

9. Masoud A. Tectonic architecture through Landsat-7 ETM+/SRTM DEM-derived lineaments and relationship to the hydrogeologic setting in Siwa Region, NW Egypt / A. Masoud, K. Koike // Journal of African Earth Sciences. — 2006. — Vol. 45, № 4–5. — P. 467–477. — DOI: 10.1016/j.jafrearsci.2006.04.005.

10. Jaireth S. Basin-related uranium mineral systems in Australia: A review of critical features / S. Jaireth, I.C. Roach, E. Bastrakov [et al.] // Ore Geology Reviews. — 2016. — Vol. 76. — P. 360–394. — DOI: 10.1016/j.oregeorev.2015.08.006.

 © Authors of the article / Authors of the article

11. Wopfner H. Tectonic and climatic events controlling deposition in Tanzanian Karoo basins / H. Wopfner // Journal of African Earth Sciences. — 2002. — Vol. 34, № 3–4. — P. 167–177. — DOI: 10.1016/S0899-5362(02)00016-7.

12. Landsat Collection 2 Level-2 Science Products : Product Guide / U.S. Geological Survey (USGS). — Reston, VA, 2023. — URL: https://www.usgs.gov/landsat-missions/landsat-collection-2-level-2-science-products (accessed: 12.11.2026)

13. QGIS Geographic Information System, Version 3.34 LTR / QGIS Development Team. — Open Source Geospatial Foundation, 2024. — URL: https://qgis.org (accessed: 26.08.2026).

14. Rowan L.C. Lithologic mapping in the Mountain Pass, California area using Advanced Spaceborne Thermal Emission and Reflection Radiometer (ASTER) data / L.C. Rowan, J.C. Mars // Remote Sensing of Environment. — 2003. — Vol. 84, № 3. — P. 350–366.

15. Nash D.J. Geochemical Sediments and Landscapes / D.J. Nash, S.J. McLaren. — Oxford: Blackwell, 2007. — 464 p.

16. Bonham-Carter G.F. Geographic Information Systems for Geoscientists: Modelling with GIS / G.F. Bonham-Carter. — Oxford: Pergamon / Elsevier Science, 1994. — 398 p.

17. Carranza E.J.M. Geochemical Anomaly and Mineral Prospectivity Mapping in GIS / E.J.M. Carranza // Handbook of Exploration and Environmental Geochemistry. — Amsterdam: Elsevier, 2008. — Vol. 11. — 351 p.

18. Cuney M. Evolution of uranium fractionation processes through time: driving the secular variation of uranium deposit types / M. Cuney // Economic Geology. — 2010. — Vol. 105, № 3. — P. 553–569. — DOI: 10.2113/gsecongeo.105.3.553.

19. Hung L.Q. Lineament extraction and analysis, comparison of LANDSAT ETM and ASTER imagery / L.Q. Hung, O. Batelaan, F. De Smedt // Remote Sensing for Environmental Monitoring, GIS Applications, and Geology V / ed. M. Ehlers. — Bellingham: SPIE, 2005. — Vol. 5983. — Art. 59830T. — (Proceedings of SPIE). — DOI: 10.1117/12.627699.

20. Gabr S. Detecting areas of high-potential gold mineralization using ASTER data / S. Gabr, A. Ghulam, T. Kusky // Ore Geology Reviews. — 2010. — Vol. 38, № 1–2. — P. 59–69. — DOI: 10.1016/j.oregeorev.2010.05.007.

21. Pour A.B. Identification of hydrothermal alteration minerals for exploring porphyry copper deposits using ASTER data, SE Iran / A.B. Pour, M. Hashim // Journal of Asian Earth Sciences. — 2011. — Vol. 42, № 6. — P. 1309–1323.

22. Phiri T. Geological and geochemical characterisation of uranium occurrences in the Kayelekera area, Malawi / T. Phiri, E.M. Tembo, C. Mutale // Journal of African Earth Sciences. — 2020. — Vol. 162. — Art. 103722. — DOI: 10.1016/j.jafrearsci.2019.103722.

23. Janeczek J. Structural formula of uraninite / J. Janeczek, R.C. Ewing // Journal of Nuclear Materials. — 1992. — Vol. 190. — P. 128–132. — DOI: 10.1016/0022-3115(92)90083-Y.

24. Burns P.C. The crystal chemistry of uranium / P.C. Burns // Reviews in Mineralogy. — 1999. — Vol. 38. — P. 23–90.

25. Grenthe I. Uranium / I. Grenthe, J. Fuger, R.J.M. Konings [et al.] // The Chemistry of the Actinide and Transactinide Elements / ed. L.R. Morss, N.M. Edelstein, J. Fuger. — Dordrecht: Springer, 2006. — P. 253–698.